A near-wall domain decomposition approach in application to turbulent flow in a diffuser

DOI:
10.1016/j.apm.2015.05.011

Document Version
Accepted author manuscript

A near-wall domain decomposition approach in application to turbulent flow in a diffuser

Adam Jones[a,*], Sergey Utyuzhnikov[a]

[a]*School of Mechanical, Aerospace and Civil Engineering, University of Manchester, Manchester, M13 9PL, UK*

Abstract

Turbulent flow in an asymmetric, two-dimensional diffuser is studied using a near-wall domain decomposition method and a $k-\varepsilon$ turbulence model. A one-dimensional boundary layer equation is used to transfer the boundary conditions from the wall to an interface within the flow. The boundary conditions applied to the fluid velocity and turbulent kinetic energy are of Robin type. They are mesh independent and can account for arbitrary source terms. This approach avoids the computational expense of fully simulating the turbulent boundary layers. For the first time, the technique has been applied to modelling a separated flow with an unstructured code. It is shown how the interface boundary condition on the turbulent kinetic energy allows the recirculation region in the diffuser to be captured. In contrast, the standard wall function approach, based on the log law, fails to predict any recirculation region. The only parameter required to apply the domain decomposition method is a turbulent viscosity profile across the boundary layer. Three different profiles are used in this work. It is shown how making the turbulent viscosity a function of the pressure gradient improves flow predictions for the diffuser. The results demonstrate that the method is an efficient way to simulate the boundary layers in engineering problems that include complex geometries or separating flows.

Keywords: Domain decomposition, Robin boundary condition, Wall functions, Turbulence, Impinging jet, Diffuser

1. Introduction

Simulation of wall-bounded turbulent flows is computationally expensive because it requires resolution of turbulent boundary layers. These thin, near-wall regions next to the laminar sublayer are always present because of the no-slip boundary condition and the damping effect of the wall. A fine mesh is required to capture the large gradients that occur in these regions. The structure of turbulent boundary layers can be resolved with low Reynolds number (LRN) turbulence models, whose governing equations remain valid to the wall. The name comes from the low turbulent Reynolds number in the boundary layer. Damping functions are often introduced into the turbulence equations to generate the

*Corresponding author. Tel.:+44 161 306 3707
Email address: adam.jones-2@manchester.ac.uk (Adam Jones)

appropriate wall-limiting behaviour of each function. However, resolution of the turbulent boundary layers can account for over 90% of the total run time of a simulation, which makes LRN models unappealing for industrial applications.

The alternative is not to fully resolve the boundary layer. This is the approach taken by high Reynolds number (HRN) models, which typically utilise wall functions. Wall functions use empirical correlations or results from simplified test cases to compute boundary conditions at the wall that account for the variation in the flow across the boundary layer. The empirical correlations are also used to compute any other required terms, such as the production of turbulent kinetic energy. With such an approach, the computational mesh can be coarse near to the wall, which makes HRN models more efficient than LRN models. However, typically their accuracy is reduced and often the assumptions upon which wall functions are derived only apply in certain types of flow.

The earliest wall function was based on the logarithmic law of the wall, which assumes that the turbulence is in local equilibrium in the turbulent region of the boundary layer. To apply this wall function, the first near-wall computational node must lie within the fully turbulent region. This requirement is often impossible to satisfy in three-dimensional flows and leads to mesh-dependent solutions. The scalable wall function [1] is an early attempt to improve the range of validity of the log law. In this approach, if the first computational node lies within the viscous sublayer, the boundary conditions are applied as if the computational node were at the edge of the viscous sublayer. However the wall function lacks generality; a general wall function must be able to handle source terms in the momentum equations.

A more sophisticated wall function is the analytical wall function [2]. This is based upon analytical integration of simplified boundary-layer equations over each near-wall cell. It does not use the log law assumption. Integration is made possible by assuming that the turbulent viscosity varies linearly from the edge of the viscous sublayer up to the far edge of the near-wall cell. Another development is the numerical wall function [3], which solves a one-dimensional transport equation over a near-wall sub-grid that spans the near-wall cell. Convection and low-Reynolds-number terms can be included in the governing equations. Both approaches specify a Dirichlet boundary condition at the first near-wall cell, which is updated at each iteration with information from the mean flow. This can be interpreted as a domain decomposition approach, with one domain limited by the centre of the cell nearest to the wall. The analytical and numerical wall functions predict complex flows with more accuracy than the log law, however they have not been widely adopted in industry because implementation of them into industrial codes requires significant changes to the code and does not generalise well to unstructured solvers.

The compound wall treatment [4] uses a one-dimensional boundary layer equation and includes source terms as a single parameter that is assumed constant over the sublayer. The solutions in the viscous and turbulent region are blended together to make the wall function valid at all points in the boundary layer. Although easy to implement and robust for industrial applications, this approach lacks validity and accuracy in complex flows, owing to its underlying assumptions.

Another class of wall function uses look-up tables for the wall shear stress. The look-up table is generated by solving simplified boundary layer equations in the absence of source terms [5]. The principle of "wall layer universality" underpins this method, which does not, in general, hold. Furthermore it is unclear how the method can be extended to handle source

terms.

This work uses the theory of interface boundary conditions (IBCs) [6–10]. This approach was first based on the same assumptions as the analytical wall function [2], but has been developed into a domain decomposition method which is applicable for LRN turbulence models.

To derive IBCs, a one-dimensional boundary layer equation is assumed to hold over the near-wall region, with Dirichlet or Neumann conditions applied at the wall. The boundary layer equation is used to transfer the boundary conditions from the wall to a location at an interface above the wall, within the fluid domain. The result is always a boundary condition of Robin type at the interface. The Robin boundary condition removes the need to compute the near-wall region of the flow. All flow variables, including velocities, scalars and turbulence functions can be treated with this approach. This produces an appealing, unified treatment. The only free parameter in the method is the turbulent viscosity profile, which is applied in the near-wall boundary layer equation. Once a converged solution is reached, the solution across the boundary layer can be found by a separate calculation, if it is required.

Wall functions are often formulated in terms of mesh parameters such as the volume of the near-wall cell [2, 3]. In contrast, IBCs are derived in a mesh-independent form and source terms can be incorporated in the boundary layer equation.

IBCs have been successfully applied to the case of a one-dimensional channel flow with two different viscosity profiles [7, 10]. In each case the results show little sensitivity to the distance from the wall. The method has also been applied in a structured code to a two-dimensional impinging jet flow [8, 9].

For flows in complex geometries, non-local effects can be important. IBCs can be generalised into a non-local formalism via the theory of Calderón-Ryaben'kii potentials [9]. This is outlined for a two-dimensional model equation in [11].

There is a trade-off between accuracy and efficiency with all near-wall modelling. A fully resolved LRN solution will always be accurate to the maximum extent possible with the chosen turbulence model, whereas a HRN solution with the log law-based wall function will produce inaccurate results in all but the simplest of flows. However, the LRN solution may require an order of magnitude more CPU time to converge [3]. IBCs are appealing because complex physics can be included in the governing equations and a good enough solution obtained across the boundary layer for a small computational cost.

LRN turbulence models can be used with IBCs [10]. In such cases, as the interface approaches the wall, the IBCs tend to the usual wall boundary conditions. Alternatively, if the interface is sufficiently far away from the wall then a HRN model emerges. This makes mesh generation simpler since the mesh in the outer region is independent of the inner region.

In this paper, IBCs have been implemented into an unstructured code for the first time. The chosen code is *Code_Saturne*, which is an open-source, industrial code developed by EDF R&D. For the first time, IBCs have been applied to a separating flow in a complex geometry. The method has been applied to a test case of an axisymmetric two-dimensional impinging jet and then to the case of a two-dimensional asymmetric diffuser. Three different viscosity profiles have been tested. Their performance on the two flows is discussed in detail.

Details of the computational code and the implementation of IBCs are given in Section 2, before a derivation of IBCs is given in detail in Section 3. Section 4 presents a discussion of the three turbulent viscosity profiles tested in this work. A comparison between IBCs

and other near-wall treatments is given in Section 5. The test case of an impinging jet is discussed in Section 6 and the two-dimensional diffuser is discussed in Section 7.

2. Computational models and code

The work was performed using *Code_Saturne* [12], which is based on a finite-volume scheme with an unstructured mesh arrangement. All variables are assigned to cell centres. Gradients are calculated with an iterative reconstruction scheme. Convection terms are calculated using a second order centered scheme. The pressure correction is accomplished with a fractional step method, based on the SIMPLEC algorithm, with Rhie and Chow interpolation to avoid chequerboard oscillations. The linear systems are solved with the Jacobi method, except for the pressure, which is solved with the conjugate-gradient method.

Boundary conditions are imposed at external faces with the specification

$$\phi^* = A_\phi + B_\phi \phi_I, \tag{1}$$

where the subscript I refers to the projection of the cell-centre onto a line normal to the boundary face. This allows the boundary conditions to be imposed at least partly implicitly.

In incompressible Reynolds-averaged Navier-Stokes simulations, the momentum, energy and many turbulence model function equations have the following form

$$\rho \frac{\partial \Phi}{\partial t} + \rho \frac{\partial (U_i \Phi)}{\partial x_i} = \frac{\partial}{\partial x_i} \left(\Gamma_\Phi \frac{\partial \Phi}{\partial x_i} \right) + F_\Phi, \tag{2}$$

where, Φ is the dependent variable, F_Φ contains any source terms and pressure gradients and

$$\Gamma_\Phi = \frac{\mu}{\sigma_\Phi} + \frac{\mu_t}{\sigma_{t,\Phi}}, \tag{3}$$

is the diffusion coefficient for Φ, where μ is the dynamic viscosity, μ_t it the turbulent viscosity, σ is the Prandtl number and σ_t is the turbulent Prandtl number. In Equation (2), Φ could be a velocity component, U, V, W, or a turbulence model function such as the turbulent kinetic energy, k. The boundary condition at the wall is often of Dirichlet type, with a value Φ_W imposed.

All IBC calculations are implemented using the standard HRN $k-\varepsilon$ model in *Code_Saturne*. For an incompressible flow the k and ε equations are

$$\frac{\partial}{\partial t}(\rho k) + \frac{\partial}{\partial x_i}(\rho U_i k) = \rho \mathcal{P} - \rho \varepsilon + \frac{\partial}{\partial x_i} \left(\left(\mu + \frac{\mu_t}{\sigma_k} \right) \frac{\partial k}{\partial x_i} \right), \tag{4}$$

$$\frac{\partial}{\partial t}(\rho \varepsilon) + \frac{\partial}{\partial x_i}(\rho U_i \varepsilon) = c_{\varepsilon 1} \frac{\rho \mathcal{P} \varepsilon}{k} - c_{\varepsilon 2} \rho \frac{\varepsilon^2}{k} + \frac{\partial}{\partial x_i} \left(\left(\mu + \frac{\mu_t}{\sigma_\varepsilon} \right) \frac{\partial \varepsilon}{\partial x_i} \right). \tag{5}$$

The production term is calculated as

$$\mathcal{P} = \mu_t \left(\frac{\partial U_i}{\partial x_j} + \frac{\partial U_j}{\partial x_i} \right) \frac{\partial U_i}{\partial x_j}, \tag{6}$$

and the turbulent viscosity is calculated as

$$\mu_t = c_\mu \rho \frac{k^2}{\varepsilon}. \tag{7}$$

The model constants are $c_\mu = 0.09$, $c_{\varepsilon 1} = 1.44$, $c_{\varepsilon 2} = 1.92$, $\sigma_k = 1$ and $\sigma_\varepsilon = 1.3$.

3. Derivation of interface boundary conditions

Interface boundary conditions are derived from one-dimensional boundary-layer type equations of the form

$$\frac{\partial}{\partial y}\left(\Gamma_\Phi \frac{\partial \Phi}{\partial y}\right) = R_\Phi, \tag{8}$$

applied in the near-wall regions of a flow. The coordinate y is understood to be the local wall-normal direction. Equation (8) follows from Equation (2) by ignoring the time derivative, convection terms and wall-parallel diffusion. In principle, the discarded terms from Equation (2) can also be included approximately in R_Φ, however in boundary layers these terms are often small and can be ignored. All source terms are included in R_Φ. For example, for the wall-parallel velocity, U, the right hand side can be approximated as the wall-parallel pressure gradient to good-enough accuracy. This can be assumed to be constant, such that

$$R_U = \left.\frac{\partial P}{\partial x}\right|^*, \tag{9}$$

where the superscript $*$ indicates that the quantity is evaluated at the interface. However for k a variable form of R_k must be used. The procedure is explained in Section 3.1.

Following [6, 8], Equation (2) is solved over a domain $\Omega := [0, y_e]$ with a wall at $y = 0$, at which a Dirichlet boundary condition is applied: $\Phi(y = 0) = \Phi_W$. The solution is built up via a domain decomposition. The domain is split into two regions: a near-wall region $\Omega_w := [0, y^*]$ and an outer region, $\Omega_e := [y^*, y_e]$. Equation (2) is solved only in Ω_e. In Ω_w, Equation (8) is used to transfer the boundary conditions from $y = 0$ to $y = y^*$. This is done with two integrations. The first integration is between limits at y and y^*:

$$\Gamma_\Phi(y)\frac{\partial \Phi}{\partial y} = \Gamma^*_\Phi \left.\frac{\partial \Phi}{\partial y}\right|^* - \int_y^{y^*} R_\Phi d\xi. \tag{10}$$

The second integration has limits at the wall and y^*. The Dirichlet boundary condition at the wall is used to arrive at

$$\Phi^* = \left.\frac{\partial \Phi}{\partial y}\right|^* \int_0^{y^*} \frac{\Gamma^*_\Phi}{\Gamma_\Phi(y)} dy - \int_0^{y^*} \frac{\int_y^{y^*} R_\Phi d\xi}{\Gamma_\Phi(y)} dy + \Phi_W, \tag{11}$$

which is a Robin type boundary condition on Φ that is applicable at y^*. Equation (11) can be compactly written as

$$\Phi^* = f_1 \Phi^*_y + \tilde{f}_2, \tag{12}$$

where the subscript y denotes differentiation with respect to y and

$$f_1 = \int_0^{y^*} \frac{\Gamma^*_\Phi}{\Gamma_\Phi(y)} dy, \tag{13}$$

$$\tilde{f}_2 = -\int_0^{y^*} \frac{\int_y^{y^*} R_\Phi d\xi}{\Gamma_\Phi(y)} dy + \Phi_W. \tag{14}$$

Equation (12) is used as a Robin boundary condition at y^* for the governing equation (Equation (2)) in Ω_e. The procedure can be followed for any fluid property to provide the necessary boundary conditions. The above procedure is used to apply boundary conditions for U, k and the temperature T. In this work, the temperature obeys a Dirichlet boundary condition at the wall. However, the above procedure can be modified for cases when a function obeys Neumann boundary conditions at the wall [6].

The k and ε equations are coupled, and so require special treatment. This is described below for the k and ε equations of the $k-\varepsilon$ model.

3.1. Boundary conditions for the $k-\varepsilon$ model

The right hand side of the k equation varies with distance from the wall. The dominant terms are the dissipation, ε, and production term, $\mathcal{P}$, as $R_k = \varepsilon - \mathcal{P}$.

A functional form of ε is prescribed following the procedure used in [2]

$$\varepsilon(y) = \frac{(k^*)^{3/2}}{c_l \max(y, y_d)}, \tag{15}$$

where $y_d = 2c_l\mu/(\rho\sqrt{k^*})$ and $c_l = \kappa/c_\mu^{3/4} = 2.55$. For $y^* > y_d$ and $y > y_d$ the dissipation varies inversely with distance from the wall. For $y^* > y_d$ and $y < y_d$ the dissipation is constant and equal to the wall-limiting value $2\mu k^*/(\rho y_d^2)$. The point y_d is within the viscous sublayer [2] which means that if $y^* < y_d$ then the interface is located in the viscous sublayer and a LRN turbulence model should be used with a modified profile of ε [10]. However in this work the condition $y^* > y_d$ is always satisfied.

The production term is calculated as

$$\mathcal{P} = -\overline{uv}\frac{\partial U}{\partial y} = \frac{\mu_t}{\rho}\left(\frac{\partial U}{\partial y}\right)^2, \tag{16}$$

which requires knowledge of the velocity gradient in Ω_w. This follows directly from Equation (10) as

$$\frac{\partial U}{\partial y} = \frac{\Gamma_U^*}{\Gamma_U(y)}\left.\frac{\partial U}{\partial y}\right|^* - \frac{\int_y^{y^*} P_x d\xi}{\Gamma_U(y)}. \tag{17}$$

Therefore the full variation of R_k is known in Ω_w and a Robin boundary condition can be calculated for k of exactly the same form as Equation (12). The dissipation is given a Dirichlet boundary condition, using Equation (15).

3.2. Boundary conditions for the wall-normal velocity and pressure

In any flow, the continuity equation demands that mass is conserved. There is no way to account for continuity with IBCs. In [8, 10], a Robin boundary condition is applied on both the wall-parallel, U, and wall-normal, V, velocity components. This produces an appealing, uniform treatment for all parameters, excluding ε. When implemented into *Code_Saturne*, the Robin boundary condition on V was found to be numerically unstable. Large mass fluxes developed across the interface boundary, which often led to the non-physical situation where more fluid leaves the computational domain through the interface than enters through the inlet. In other cases, the interface became an inlet and more fluid left through the outlet

than entered through the real inlet. It seems that this behaviour is related to the particular implementation of boundary conditions in *Code_Saturne*, which is not always robust. To avoid this behaviour, the boundary condition for V was modified. A dynamic pressure term was introduced in the boundary layer so that $P \propto y^4$. Then, V is solved for by taking $R_V = 4Ky^3$ and integrating Equation (8) from the wall twice, and applying the boundary conditions $V(0) = 0$ and $V_y(0) = 0$. The result is a Dirichlet boundary condition at the interface

$$V^* = K \int_0^{y^*} \frac{\xi^4 d\xi}{\mu + \mu_t(\xi)}, \tag{18}$$

where the normalisation constant is

$$K = \int_0^{y_I} \frac{\xi^4 d\xi}{\mu + \mu_t(\xi)}, \tag{19}$$

where $y_I > y^*$ is the distance normal to the wall of the cell centre next to the interface. This ensures that V is continuous across both Ω_w and Ω_e. Equation (18) limits V in Ω_w to the interval $[0, V^*]$. This prevents the pressure correction algorithm in Ω_e from calculating non-physical mass fluxes.

4. The near-wall turbulent viscosity profile

The only parameter needed to apply the boundary conditions in Equation (12) at y^* is an approximation for the variation of μ_t in Ω_w. The original log law-based wall function was derived on the physical assumption that the turbulent length scale, l, varies with distance from the wall, y as $l = \kappa y$, with $\kappa = 0.41$ called the von Kármán constant. This work uses more sophisticated assumptions. The three turbulent viscosity profiles that are used in this work are described below. They are:

1. A piecewise linear profile:

$$\mu_t(y) = \max\left(0, \frac{y - y_v}{y^* - y_v}\mu_t^*\right), \tag{20}$$

   where $y_v = Re_v\,\mu/(\rho\sqrt{k^*})$ represents the edge of the viscous sublayer. The value of the free parameter $Re_v = 10.8$ is consistent with [2].
   An advantage of this profile is that μ_t is totally determined by the solution in Ω_e. It has been widely tested already with IBCs on an impinging jet flow [9], and in a channel flow [7]. It is similar to the profile used in the analytical wall function [2], however in that case μ_t is not continuous at y^*.
2. A non-linear, exponential profile used in [13] that resembles a van Driest damping function [14]:

$$\mu_t(y) = \mu\kappa y^+ \left(1 - \exp(-y^+/A^+)\right)^2, \tag{21}$$

   with $A^+ = 19$, $\kappa = 0.41$ and the definitions $y^+ = yu_\tau\rho/\mu$ and $u_\tau = \sqrt{\tau_w/\rho}$, where τ_w is the wall shear stress. The parameter τ_w is not known a priori and must be calculated at each iteration using Equation (10). Furthermore, continuity of μ_t is not guaranteed at y^*. This profile has already been used with IBCs on a channel flow [10] and has been widely used to develop wall models for large-eddy simulations.

3. The non-linear profile of Duprat et al. [15], which is sensitised to the pressure gradient:

$$\mu_t(\xi) = \mu\kappa\xi^* \left[\alpha + \xi^* (1-\alpha)^{\frac{3}{2}}\right]^{\beta} \left(1 - \exp\left(\frac{-\xi^*}{1 + A\alpha^3}\right)\right)^2, \tag{22}$$

where ξ has been used instead of y to avoid confusion with the IBC parameter y^*. Equation (22) uses the parameters $\kappa = 0.41$, $A = 17$ and $\beta = 0.78$, and the definitions $\alpha = u_\tau^2/u_{\tau p}^2$ and $\xi^* = y u_{\tau p}/\nu$, where

$$u_{\tau p} = \sqrt{u_\tau^2 + u_p^2}, \tag{23}$$

and

$$u_p = \left|\frac{\mu}{\rho^2}\frac{\partial p}{\partial x}\right|^{\frac{1}{3}}. \tag{24}$$

This viscosity profile was developed to improve the predictions of the van Driest damping function [14] in flows where the pressure gradient is significant; for example, in separating flows. The main advantage is that it can be applied at separation points, where the van Driest damping function fails to predict any turbulence. As with the van Driest damping functions, μ_t is not continuous at y^*. When used as a near-wall model for large-eddy simulation, this profile made accurate predictions of the location of the separation and reattachment points in a flow over periodic hills [15].

5. Comparison with other near-wall treatments

It is useful to compare IBCs to the analytical (AWF) [2] and numerical (NWF) [3] wall functions because they share some assumptions. For example, all three methods use a governing equation that can be written in the form of Equation (8).

IBCs can account for arbitrary source terms or variations of fluid properties. However, the AWF requires modification when analytical integration is not possible. For example, the variation of laminar viscosity in a buoyant flow must be fit to an analytical curve. A piecewise linear approximation of this variation was found to be unstable with the AWF. This was due to the discontinuous first derivative of μ causing a singularity in the boundary layer equation. With IBCs, no such instability would be encountered because the boundary conditions are calculated entirely by integration.

IBCs can be formulated for LRN turbulence models [10]. This is also possible for the NWF, but not of the AWF, where analytical integration would be impossible. This limits accuracy of the AWF in complex flows, where the requirement of a large y^+ cannot be guaranteed to hold for every near-wall cell.

The Robin boundary condition in Equation (12) is numerically robust because both a function and its derivative are specified at the same iteration. Because Equation (12) follows directly from Equation (8) and the boundary conditions, an analogous equation to Equation (12) for the velocity, U, can be written for the AWF or NWF. It reads [9]

$$U^{*(n)} = f_1 U_y^{*(n-1)} + \tilde{f}_2, \tag{25}$$

where the superscripts in parentheses refer to the iteration number. With the AWF and NWF, U_y^* is calculated from the solution at the previous iteration. Its value is then used to update U^*. Thus, in the case of the AWF and NWF, the leading term is taken from the previous iteration. Furthermore, this term is a derivative, which must be approximated. This contrast with IBCs means that the IBC approach should converge in fewer iterations, because U^* and U_y^* are taken at the same iteration.

Implementation of both the AWF and NWF requires modifications to the original code, which makes implementation of them into unstructured codes difficult or impossible. As a domain decomposition approach, the Robin boundary conditions used with IBCs can be calculated independently of the underlying code. Therefore, they can be readily applied to unstructured codes. They can be implemented with finite-volume, finite-difference or finite-element based codes.

6. An axisymmetric impinging jet test case

The axisymmetric impinging jet is a well-established test case and has been used to develop many turbulence models. It has previously been studied with IBCs in [8, 9]. This work is the first study of the jet with IBCs in an unstructured code, with three different viscosity profiles. Impinging jets are useful to study from an industrial perspective as they frequently appear in heat transfer applications. Experimental studies have been performed in [16–18].

A fully developed circular pipe flow of diameter D, in thermal equilibrium, emerges at a distance, H, above an infinite flat plate, as in Figure 1. The flat plate is kept at a constant temperature. The Reynolds number based on pipe diameter and bulk velocity in the pipe is $Re = 70,000$. Simulations were run with $H/D = 2$ and $H/D = 6$. The Nusselt number is defined as

$$Nu = \frac{q_w'' D \sigma}{\mu c_p (T_w - T_i)}, \tag{26}$$

where q_w'' is the heat flux at the wall, $\sigma = 0.71$ is the Prandtl number, c_p is the heat capacity, T_w is the wall temperature and T_i is the inlet temperature.

The inlet conditions were calculated on a very fine one-dimensional grid. For the $k - \varepsilon$ model this required use of a LRN model. The model in [19] was chosen, which solves for a function $\tilde{\varepsilon}$ which is equal to zero at the wall. The required factor of $2\nu k/y^2$ was added to $\tilde{\varepsilon}$ to convert it into the HRN function ε.

The flow domain contains a 1° sector of a cylinder. Rotational periodic boundary conditions are applied on the faces in the ϕ direction and zero-gradient conditions are imposed on the outlets at $z = H$ for $r > D/2$ and $r = L$. The length of the wall is $L = 13D$. The wall is located at $z = 0$ and the inlet at $z = H$. Since the mesh used is three-dimensional, no boundary conditions can be imposed on the axis of symmetry.

The LRN results were obtained on a fine mesh with 170 cells in the axial direction. The HRN log law results were obtained with a mesh with 120 cells in the axial direction. The IBC method was applied with the HRN $k - \varepsilon$ turbulence model, on a mesh that contained 120 cells in the axial direction. The three meshes all contained 149 cells in the radial direction. The distribution of cells in this direction was the same for each mesh so that only the axial resolution is different. The integrals for f_1 and f_2 were calculated numerically with 200

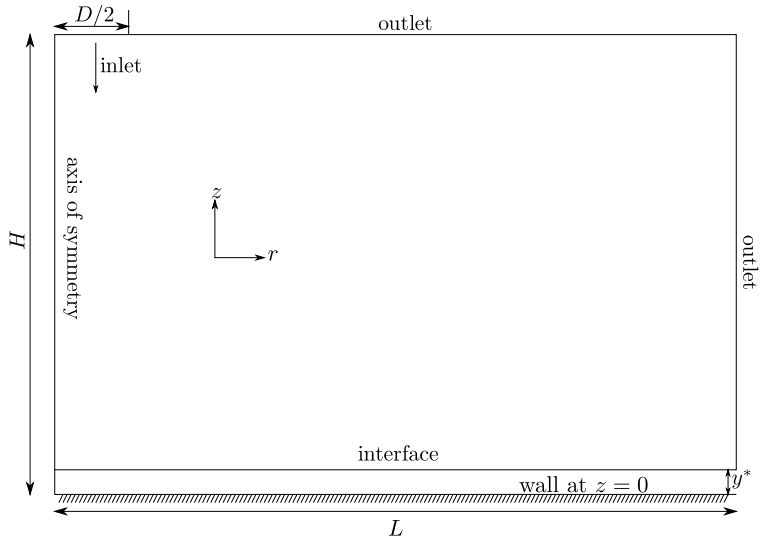

Figure 1: The impinging jet geometry.

equally-spaced nodes. The results are compared to the experimental data of [16] and [18], the standard HRN $k-\varepsilon$ model with the log law-based scalable wall function and to the LRN $k-\omega$ SST model [20]. When the number of cells in each direction was doubled, for each case, no difference was observed in any of the plots below.

6.1. Results and discussion of impinging jet test case

The Nusselt number predictions for $H/D = 2$ are shown in Figure 2a, and those for $H/D = 6$ are shown in Figure 2b. The linear viscosity profile (Equation (20)) is the only viscosity profile that predicts a reasonable value of Nu at $r = 0$. It also produces a change in curvature in Nu around $r/D \approx 1.3$ for $H/D = 2$.

The failure of the exponential and Duprat et al. [15] profiles (Equations (21) and (22), respectively) to predict the peak in Nu at the stagnation point stems from the specification of the turbulent viscosity at y^*. Both τ_w and dP/dr are zero at the stagnation point. This means that the exponential and Duprat et al. [15] profiles predict the turbulent viscosity to be zero there. The Nusselt number depends on the heat flux at the wall, $\dot{q}''_W$,

$$\dot{q}''_W = \left(\frac{\mu}{\sigma} + \frac{\mu_t}{\sigma_t}\right)\left.\frac{\partial T}{\partial y}\right|_w = \left(\frac{\mu}{\sigma} + \frac{\mu_t^*}{\sigma_t}\right)\left.\frac{\partial T}{\partial y}\right|^*, \tag{27}$$

where the last equality follows from Equation 10 since there are no source terms in the temperature equation. If μ_t^* is calculated to be zero, then the heat flux at the wall is underestimated. The linear profile uses μ_t at the cell centre to determine μ_t^*. This allows it to correctly capture the link between k and Nu, and to capture the peak in Nu at the stagnation point.

Table 1 shows the values of y^* and $Re_y^* \equiv \rho\sqrt{k^*}y^*/\mu$ at the stagnation point for the three viscosity profiles for the cases $H/D = 2$ and 6. In contrast to the Nusselt number, there is little difference between the values of Re_{y^*} for the three viscosity profiles. This is because $U_y = 0$ on the axis of symmetry so the production term is zero. Therefore the dissipation is

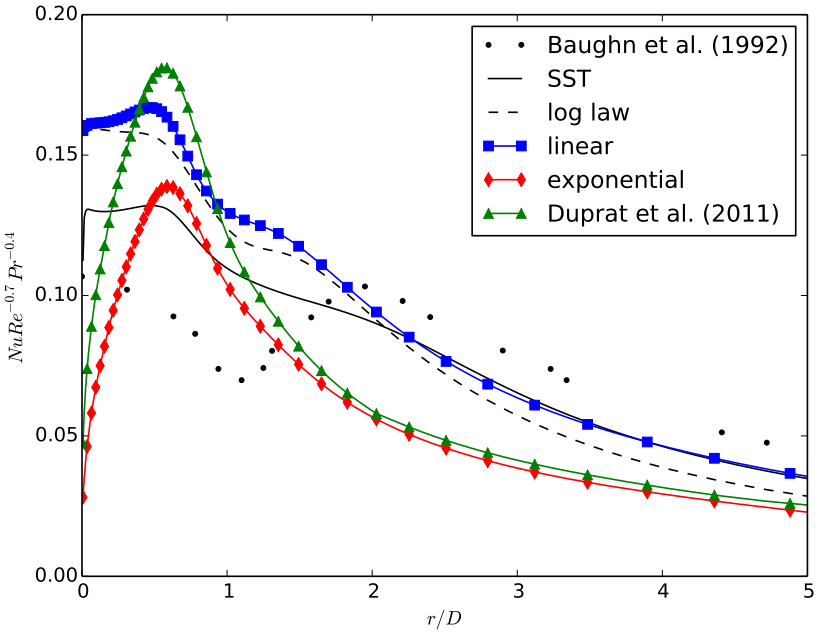

(a) $H/D = 2$

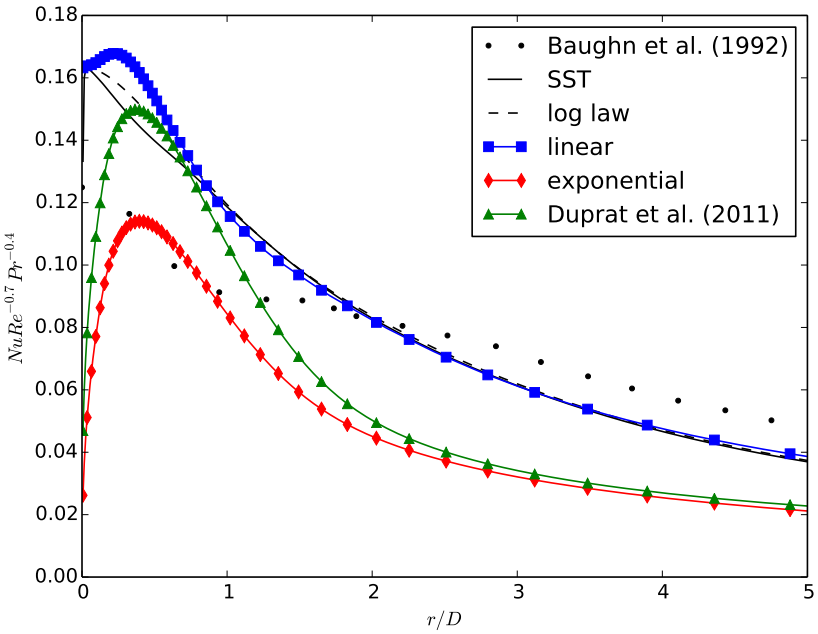

(b) $H/D = 6$

Figure 2: IBC Nusselt number predictions along the heated wall for the impinging jet compared to the experimental data of [16], the LRN $k-\omega$ SST model and the HRN $k-\varepsilon$ model with the log law-based scalable wall function.

	$H/D = 2$		$H/D = 6$	
	y^*/D	Re_{y^*}	y^*/D	Re_{y^*}
Linear	0.02	239	0.04	586
Exponential	0.02	166	0.04	452
Duprat	0.02	209	0.04	559

Table 1: y^* and $Re_{y^*} \equiv \rho\sqrt{k_I}y^*/\mu$ at the stagnation point for the impinging jet flows.

the dominant term in the k boundary layer equation, which is calculated in the same way for all three viscosity profiles.

It is well known that LRN linear eddy-viscosity models tend to over-predict the heat transfer at the stagnation point because they are unable to reproduce the flow anisotropy there [21]. This leads to large values of the production term at the stagnation point. Both the IBC formulation and log law-based wall function ignore the normal turbulent Reynolds stresses when calculating the production, therefore the over-prediction of heat transfer is not seen in Figure 2. If the normal Reynolds stresses were included in the calculation of the production, Nu would increase at the stagnation point. This happens with the NWF [3].

The speed of the fluid, normalised by the inlet bulk velocity, $\sqrt{U^2 + W^2}/U_b$, is shown at the locations $r/D = 0$, and 1 for the case with $H/D = 2$ in Figure 3. These profiles show little sensitivity to the viscosity profile. Figure 3a shows the fluid on the line of symmetry, where $U = 0$. The good enough prediction here justifies the wall-normal treatment based on $P_y = 4Ky^3$.

7. A two-dimensional asymmetric diffuser

Real engineering flows typically involve complex geometries. These geometries affect the flow physics. An example of such an effect is flow separation. It is a challenge for any near-wall model to accurately predict points of flow separation and reattachment; even for LRN turbulence models. The diffuser flow in this section exhibits flow separation caused by an adverse pressure gradient along the inclined wall. The low slope of the diffuser wall means that the separation and reattachment points can not be determined from the geometry alone. A reliable turbulence model must be able to predict the location of these two points.

The geometry of the diffuser is shown in Figure 4. The inlet is located at $x/H = -10$ and the outlet is at $x/H = 75$. The leading corner of the diffuser is centred on $x/H = 0$. Both corners of the diffuser are smoothed.

The flow was first studied experimentally in [22], however the large-eddy simulation results of [23] cast doubt on the accuracy of the experimental results, which prompted an experimental re-examination of the flow, which paid particular attention to the two-dimensionality of the problem [24].

This diffuser has been numerically studied with many turbulence models, such as the $k-\omega$, $k-\omega$ SST and LRN $k-\varepsilon$ models [25]. Further studies of the diffuser were performed in [26], where non-linear eddy-viscosity models and Reynolds stress models are used; and in [27], where the LRN $\overline{v^2} - f$ model is used.

The inlet conditions are those of a channel flow at a Reynolds number based on bulk velocity and channel height of $Re = 18,000$. As with the impinging jet, these were calculated

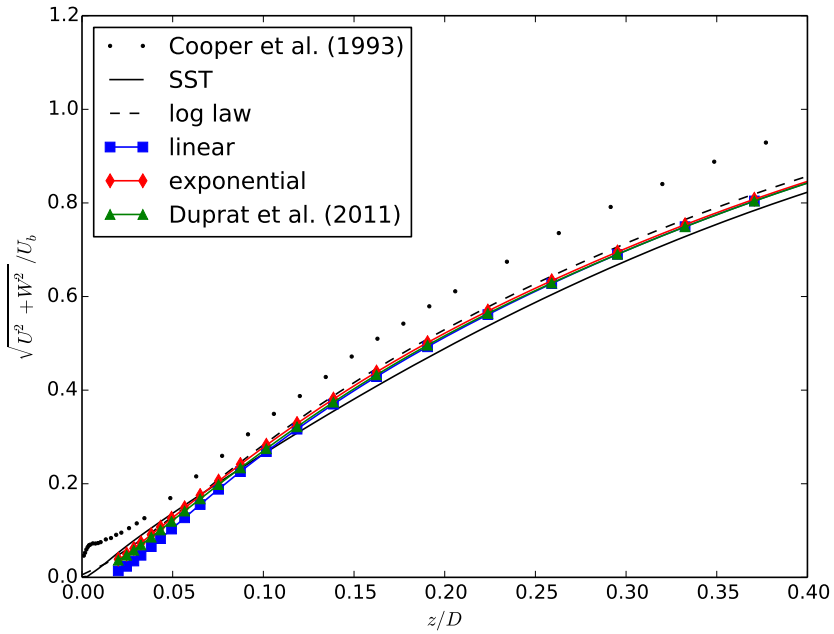

(a) $r/D = 0$

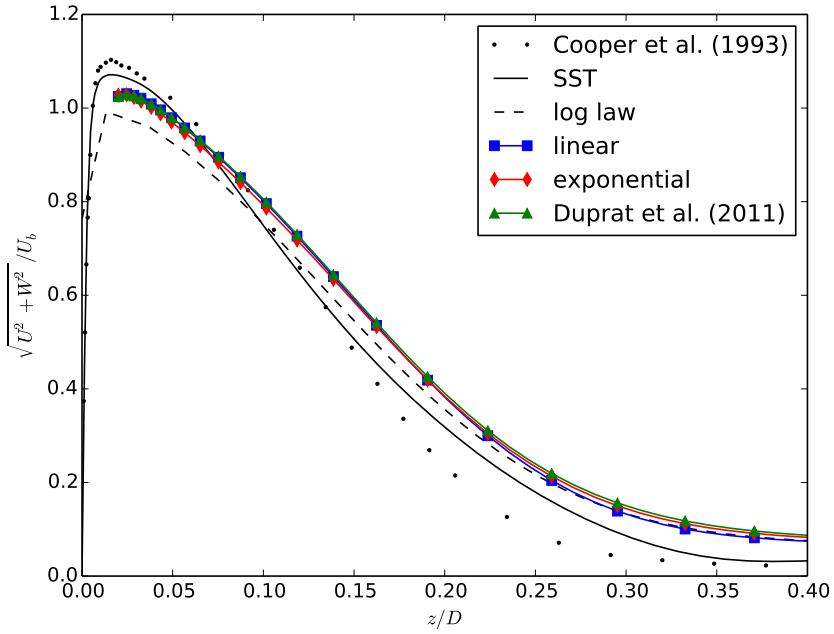

(b) $r/D = 1$

Figure 3: The normalised speed $\sqrt{U^2+W^2}/U_b$ in the impinging jet predicted by IBC calculations compared to the data of [18], the LRN $k-\omega$ SST model and the HRN $k-\varepsilon$ model with the log law-based scalable wall function, at $H/D = 2$.

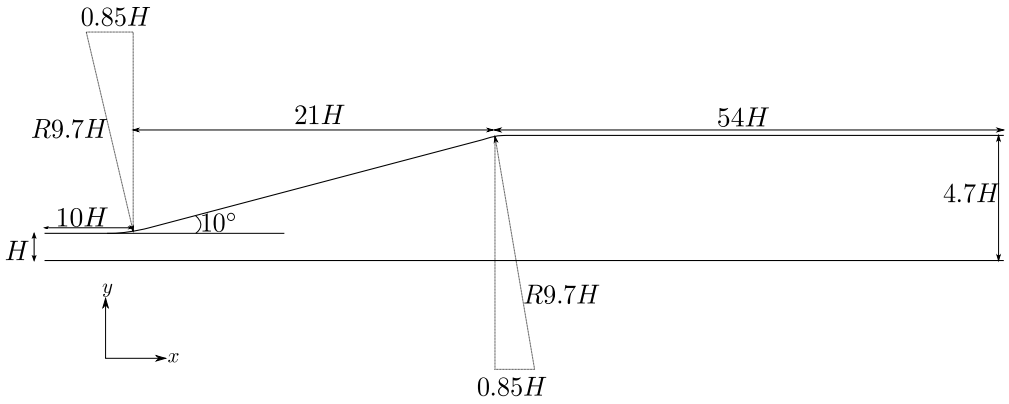

Figure 4: The geometry of the diffuser.

on a very fine one-dimensional grid with a LRN $k-\varepsilon$ model [19], with $\tilde{\varepsilon}$ corrected to be equivalent to the HRN function, ε. IBC results are compared to those obtained with the HRN $k-\varepsilon$ model with the log law-based scalable wall function, the LRN $k-\omega$ SST model and the experimental data of [24].

The LRN $k-\omega$ SST results were obtained on a fine mesh which has 140 cells in the span-wise y direction. Cells are clustered towards the wall so that the maximum value of y^+ of any near-wall cell is 0.34. The log law results are obtained on a mesh with 30 equally-spaced cells in the y direction. This gives $y^+ \in [5, 25]$ over the near-wall cells. It is not possible to satisfy $y^+ > 30$ everywhere because of the small value of τ_w along much of the diffuser body. A coarser mesh would not allow enough grid points to be able to resolve the flow features adequately. The IBC simulations are set up with an offset between the wall and the interface that is 5% of the height of the diffuser at that point. Therefore, at all points, the mesh covers 90% of the height of the diffuser. The mesh has 50 cells in the span-wise y direction. This gave $y^+ \in [3, 70]$. The integrals required for f_1 and f_2 were calculated numerically with 200 equally-spaced nodes.

All three meshes have 398 cells distributed identically in the x direction. The meshes only differ in the y direction.

In all cases, grid independence was verified by doubling the number of computational cells in each direction (except for the span-wise direction with the standard log law, where doing this would make y^+ too small). No significant change was seen in any of the results.

7.1. Diffuser results and discussion

The wall shear stress, τ_w, as calculated by Equation (10), converged slowly with the exponential viscosity profile. To speed up the convergence, τ_w was averaged at each iteration. No averaging was required for the linear and Duprat et al. [15] profiles.

The skin friction coefficient, $C_f = \tau_w/(\frac{1}{2}\rho U_b^2)$ is shown for the straight wall in Figure 5a and the inclined wall in Figure 5b.

Figure 5a shows that the linear and Duprat et al. [15] viscosity profiles correctly predict no separation along the straight wall of the diffuser. The same is also observed in the log law results. The exponential profile incorrectly predicts a recirculation region on the straight wall. This is a consequence of the exponential profile using only τ_w to determine μ_t. Because the shear stress is small along this section of the diffuser, the exponential viscosity profile

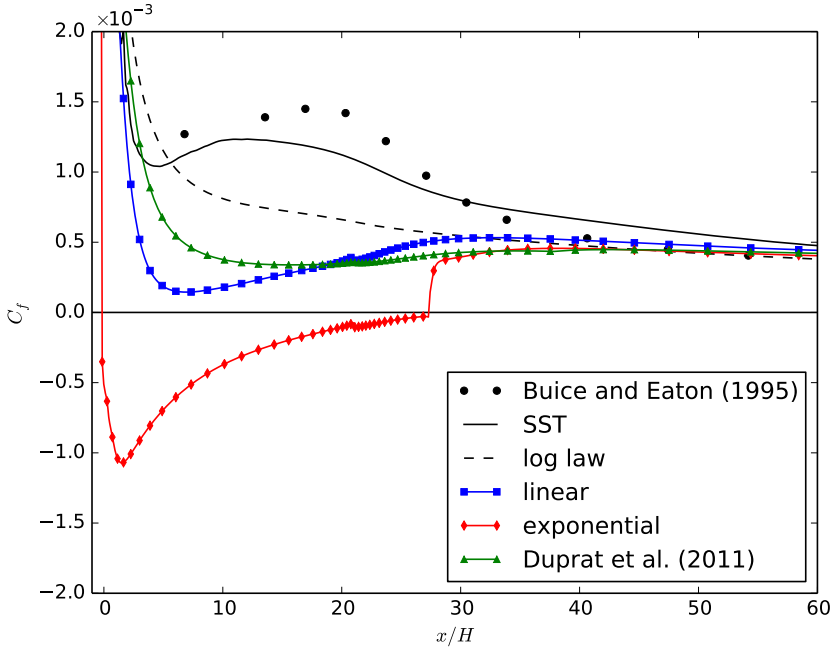

(a) Straight wall

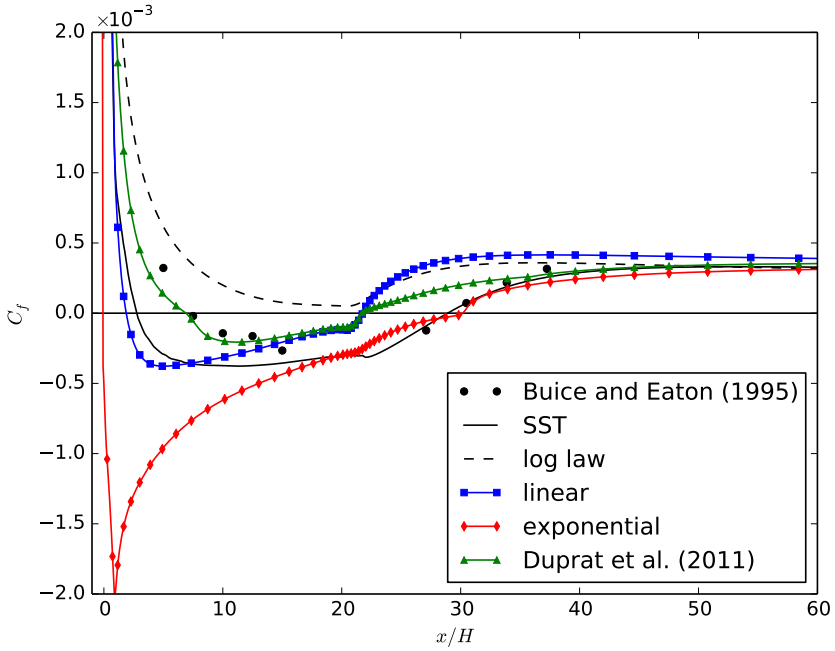

(b) Inclined wall

Figure 5: The skin friction coefficient, $C_f = \tau_w/(\frac{1}{2}\rho U_b^2)$ along the straight and inclined walls of the diffuser. The IBC results are compared to the experimental data of [24], the LRN $k-\omega$ SST model and the HRN $k-\varepsilon$ model with the log law-based scalable wall function.

under-predicts μ_t by up to an order of magnitude at y^*. With $\mu_t(y) \approx 0$, Equation (10) for the wall shear stress reduces to

$$\tau_w \approx \mu U_y^* - y^* P_x. \tag{28}$$

Since μU_y^* is often small and $P_x > 0$ in the diffuser body, the shear stress is calculated to be negative along the straight wall of the diffuser. In contrast, the linear and Duprat et al. [15] profiles are sensitised to k^* and P_x^*, respectively, which means that the two profiles predict μ_t at y^* to be close to its value in the bulk. This explains the superior predictions of these two profiles.

The secondary peak in C_f on the straight wall around $x/H \approx 15$ that is observed in the experimental data and the $k-\omega$ SST results is not present in any of the $k-\varepsilon$ results. The failure to predict this is due to the inability of the $k-\varepsilon$ model to correctly capture the flow anisotropy in the bulk.

Figure 5b shows that the IBC method predicts a recirculation region, whereas the log law fails to. The recirculation region is caused by an adverse pressure gradient, which is not accounted for by the log law-based wall function. The log law calculates τ_w as $\tau_w = \rho u_k u_\tau$. Since ρ and $u_k = c_\mu^{1/4} k^{1/2}$ are both positive, τ_w can only be negative if u_τ is negative, which requires a negative wall-parallel velocity at the near-wall cell centre. Because the recirculation region is thin, almost any reasonable size of near-wall cell will lead to $u_\tau > 0$, so τ_w will be calculated to be positive. However, the IBC approach takes the pressure gradient into account through R_U, and in the case of the Duprat et al. [15] viscosity profile, through $\mu_t(y)$. This enables the IBC results to capture the recirculation region on the inclined wall.

None of the models capture the correct size of the recirculation region, however the profile of Duprat et al. [15] predicts the separation point to be in almost exactly the same location as the experimental data. The exponential viscosity profile makes the most accurate prediction of the reattachment point, which occurs in the channel section of the diffuser. The $k-\omega$ SST model also predicts the reattachment point well. Both the linear and Duprat et al. [15] profiles predict reattachment to occur at the second corner of the diffuser, at $x/H \approx 21$. Spurious behaviour is also visible at $x/H \approx 21$ along the straight wall in Figure 5a for these two profiles. Non-local effects are important at this point, but are not accounted for with the one-dimensional boundary layer equation. A two-dimensional boundary layer equation that includes non-local effects would perform better here, and could be implemented with the theory of non-local wall functions [11].

Previous studies have shown that the $k-\varepsilon$ model performs poorly on this flow. The LRN $k-\varepsilon$ model of [28] fails to predict any recirculation region [25]. IBCs predict a recirculation region because the $k-\varepsilon$ model is not used in the boundary layer. Instead a simple one-equation turbulence model is used, with the turbulent viscosity specified algebraically. This allows for more detailed physics to be captured in the boundary layers by modifying the turbulent viscosity profile.

The pressure coefficient is calculated as $C_P = (P - P_{\text{ref}})/(\frac{1}{2}\rho U_b^2)$, where the reference pressure, P_{ref}, is the pressure at $x/H = -1.7$. It is shown for the straight wall in Figure 6a and the inclined wall in Figure 6b. The predictions of C_P with IBCs compare well to the predictions with the log law, however none of the $k-\varepsilon$ models are able to capture the change in the curvature of C_P at the diffuser outlet entrance, which is captured by the $k-\omega$ SST model. Since the pressure is calculated only within Ω_e, the form of C_P with IBCs is similar

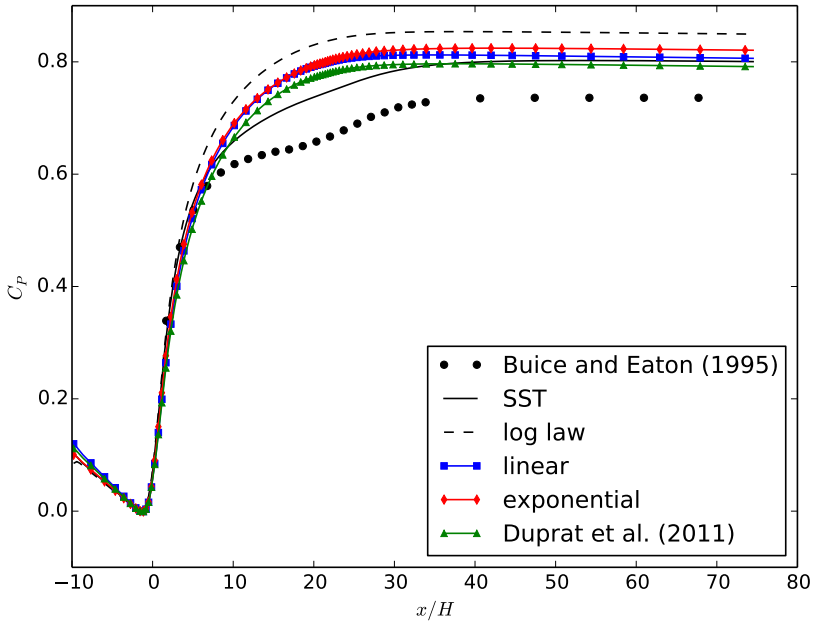

(a) Straight wall

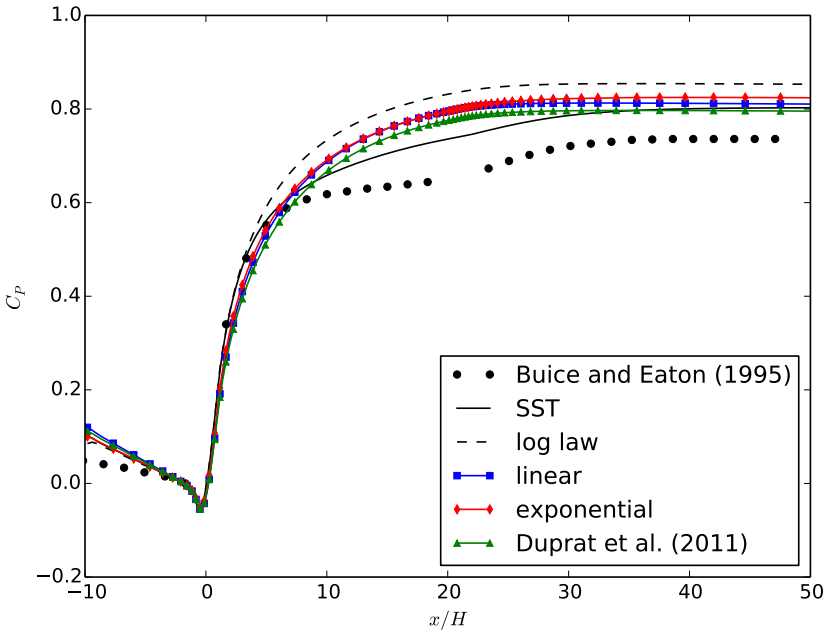

(b) Inclined wall

Figure 6: The pressure coefficient, C_P, for the diffuser along the straight and inclined walls. The IBC results are compared to the experimental data of [24], the LRN $k-\omega$ SST model and the HRN $k-\varepsilon$ model with the log law-based scalable wall function.

that with the log law wall function because the governing equations are the same in Ω_e. Hence the failure to capture the curvature in C_P with IBCs is due to the deficiencies of the underlying $k-\varepsilon$ model. If IBCs were applied to the $k-\omega$ SST model, this curvature could be captured. The pressure drops across the whole diffuser are slightly more accurate for all results with IBCs than for the standard log law because the results with IBCs predict τ_w more accurately. In the case of the Duprat et al. [15] viscosity profile, the total pressure drop is almost identical to the $k-\omega$ SST result.

7.2. The effect of the Robin boundary condition on k

Instead of the Robin boundary condition of Equation (12), a Dirichlet boundary condition can be applied to k using the specified profiles of μ_t and ε:

$$k^* = \sqrt{\frac{\mu_t^* \varepsilon^*}{c_\mu}}. \tag{29}$$

Because ε is specified with its equilibrium length scale, applying Equation (29) amounts to specifying k with its equilibrium length scale. Other Dirichlet conditions could be applied to k [2], however these typically require choosing ad hoc profiles for k, which are no more sophisticated than the profiles already used for ε and μ_t. Hence Equation (29) reflects the boundary condition that would be applied by a typical wall function treatment.

Another set of computations was performed on the diffuser using the Dirichlet boundary condition in Equation (29). The skin friction coefficient predictions are shown for the straight wall in Figure 7a and the inclined wall in Figure 7b. In Figure 7, the unconnected points show the results of simulations where k receives the Dirichlet boundary condition of Equation (29). The connected points show the results when k is given a Robin boundary condition (Equation (12)).

Figure 7b shows that the recirculation region vanishes for the linear viscosity profile when a Dirichlet condition is applied to k. The recirculation region remains with the Duprat et al. [15] profile because this is less sensitive to k, since $\mu_t(y)$ does not depend directly upon it. However, the size of the recirculation region is reduced. These results demonstrate that the boundary condition on k is crucial for predicting the recirculation region and further explain why the standard log law does not predict a recirculation region. In contrast to the Robin boundary condition, the equilibrium assumption of Equation (29) does not capture the flow physics that affect k in the boundary layer. The results with the exponential viscosity profile do not change significantly when the k boundary condition is altered because when $\mu_t(y)$ is small the velocity boundary conditions are determined mainly by the pressure gradient. The pressure field depends only weakly on k, hence the velocity predictions are similar to the case with a Robin boundary condition.

8. Conclusions

For the first time, IBCs have been implemented into an unstructured code and applied to a separating flow in a complex geometry. Three different viscosity profiles have been tested. The main conclusions that can be drawn from this work are summarised below.

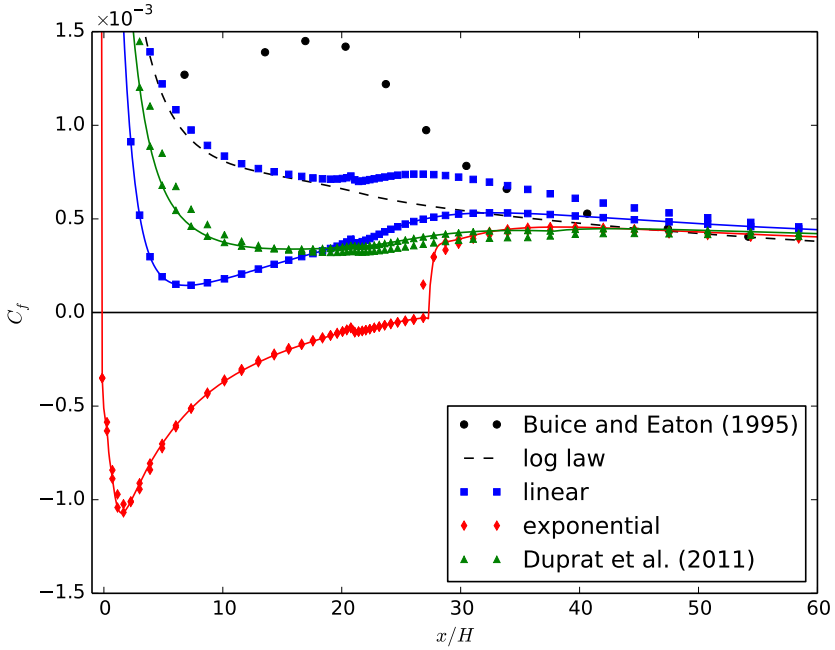

(a) Straight wall

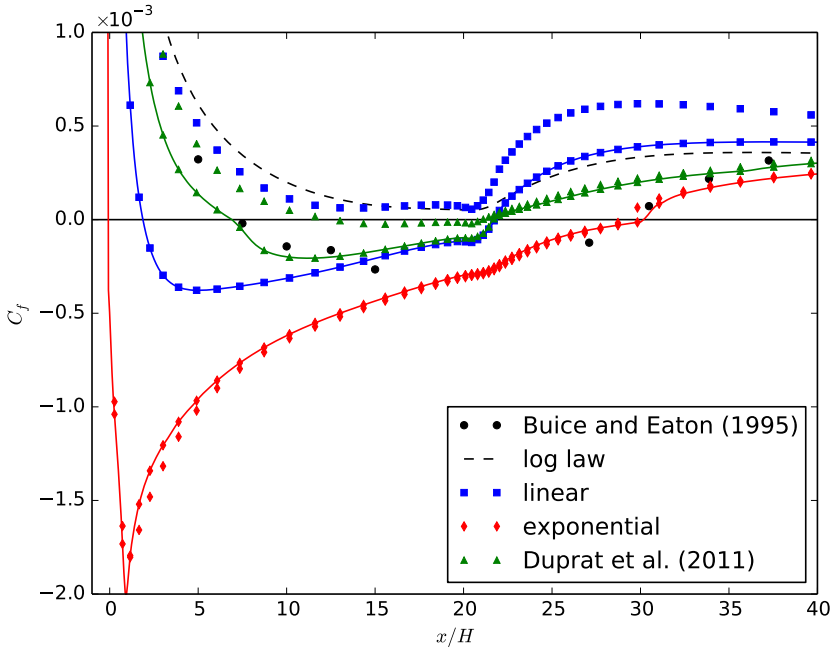

(b) Inclined wall

Figure 7: The skin friction coefficient, C_f, along the straight and inclined walls of the diffuser. The unconnected points show the results when k is given a a Dirichlet boundary condition (Equation (29)). The connected points are the results when k is given a Robin boundary condition (Equation (12)).

IBCs represent a domain decomposition approach. They can be considered as applying a different turbulence model in the near-wall region to that used in the bulk flow. In this way, IBCs can serve as a framework with which to investigate viscosity profiles and may be useful for developing new near-wall models for both LRN and HRN simulations.

Applying IBCs on k as well as U is more accurate than assuming that the turbulence is in local equilibrium in the boundary layer. With the linear viscosity profile, using a Robin boundary condition on k leads to the prediction of a recirculation region in the diffuser flow that is not present when a Dirichlet boundary condition is used. This explains why the standard log law-based wall function fails to predict a recirculation region in the diffuser flow.

The methodology outlined here seems useful for simulation of industrial flows with complex geometries. IBCs allow simulations to capture the effects of walls on the flow, without a fine mesh resolution. This leads to cost savings not just from the CPU time advantages possible with IBCs, but also from the time saved generating a mesh.

9. Acknowledgements

This work was carried out as part of a research project sponsored by EDF Energy. The first author is supported by the EPSRC and EDF Energy UK. The authors are grateful to the anonymous referees for useful remarks that allowed them to improve the quality of this paper.

References

[1] H. Grotjans, F. R. Menter, Wall functions for general application CFD codes, in: Papailou (Ed.), ECCOMAS 98, European Congress on Computational Methods in Applied Sciences and Engineering, Swansea, 1998, pp. 1112 – 1117.

[2] T. J. Craft, A. V. Gerasimov, H. Iacovides, B. E. Launder, Progress in the generalization of wall-function treatments, Int. J. Heat Fluid Fl. 23 (2) (2002) 148–160. doi:10.1016/S0142-727X(01)00143-6.

[3] T. J. Craft, S. E. Gant, H. Iacovides, B. E. Launder, A new wall function strategy for complex turbulent flows, Numer. Heat Tr. B-Fund. 45 (4) (2004) 301–318. doi:10.1080/10407790490277931.

[4] M. Popovac, K. Hanjalić, Compound wall treatment for RANS computation of complex turbulent flows and heat transfer, Flow, Turbul. Combust. 78 (2) (2007) 177–202. doi:doi:10.1007/s10494-006-9067-x.

[5] G. Kalitzin, G. Medic, G. Iaccarino, P. Durbin, Near-wall behavior of rans turbulence models and implications for wall functions, J. Comput. Phys. 204 (1) (2005) 265–291. doi:10.1016/j.jcp.2004.10.018.

[6] S. V. Utyuzhnikov, Some new approaches to building and implementation of wall-functions for modeling of near-wall turbulent flows, Comput. Fluids 34 (7) (2005) 771 – 784. doi:10.1016/j.compfluid.2004.07.004.

[7] S. V. Utyuzhnikov, Generalized wall functions and their application for simulation of turbulent flows, Int. J. Numer. Meth. Fl. 47 (10-11) (2005) 1323–1328. doi:10.1002/fld.873.

[8] S. V. Utyuzhnikov, The method of boundary condition transfer in application to modeling near-wall turbulent flows, Comput. Fluids 35 (10) (2006) 1193 – 1204. doi:10.1016/j.compfluid.2005.05.005.

[9] S. V. Utyuzhnikov, Robin-type wall functions and their numerical implementation, J. Appl. Numer. Math. 58 (10) (2008) 1521 – 1533. doi:10.1016/j.apnum.2007.09.003.

[10] S. V. Utyuzhnikov, Interface boundary conditions in near-wall turbulence modeling, Comput. Fluids 68 (2012) 186 – 191. doi:10.1016/j.compfluid.2012.07.023.

[11] S. V. Utyuzhnikov, Domain decomposition for near-wall turbulent flows, Comput. Fluids 38 (9) (2009) 1710 – 1717. doi:10.1016/j.compfluid.2009.03.003.

[12] F. Archambeau, M. Namane, M. Sakiz, Code saturne: A finite volume code for turbulent flows, International Journal on Finite Volumes 1.

[13] W. Cabot, P. Moin, Approximate wall boundary conditions in the large-eddy simulation of high Reynolds number flow, Flow, Turbul. Combust. 63 (1999) 269–291. doi:10.1023/A:1009958917113.

[14] E. R. van Driest, On turbulent flow near a wall, J. Aerosp. Sci. 23 (1956) 1007–1011.

[15] C. Duprat, G. Balarac, O. Metais, P. M. Congedo, O. Brugiere, A wall-layer model for large-eddy simulations of turbulent flows with/out pressure gradient, Phys. Fluids 23 (1) (2011) 015101. doi:10.1063/1.3529358.

[16] J. W. Baughn, X. J. Yan, M. Mesbah, The effect of Reynolds number on the heat transfer distribution from a flat plate to a turbulent impinging jet, in: ASME Winter Annual Meeting, Anaheim, California, 1992, pp. 1–7.

[17] J. W. Baughn, S. Shimizu, Heat transfer measurements from a surface with uniform heat flux and an impinging jet, J. Heat Transf. 111 (4) (1989) 1096–1098.

[18] D. Cooper, D. C. Jackson, B. E. Launder, G. X. Liao, Impinging jet studies for turbulence model assessment - I. Flow-field experiments, Int. J. Heat Mass Tran. 36 (10) (1993) 2675–2684.

[19] K.-Y. Chien, Predictions of channel and boundary-layer flows with a low-reynolds-number two-equation model of turbulence, AIAA J. 20 (1).

[20] F. R. Menter, Two-equation eddy-viscosity turbulence models for engineering applications, AIAA J. 32 (1994) 1598–1605. doi:10.2514/3.12149.

[21] T. J. Craft, L. J. W. Graham, B. E. Launder, Impinging jet studies for turbulence model assessment. Part II: An examination of the performance of four turbulence models, Int. J. Heat Mass Tran. 36 (10) (1993) 2685–2697.

[22] S. Obi, K. Aoki, S. Masuda, Experimental and computational study of turbulent separating flow in an asymmetric plane diffuser, in: Proceedings 9th Symposium of turbulent shear flow, Kyoto, Japan, 1993, pp. 305.1–305.4.

[23] H.-J. Kaltenbach, M. Fatica, R. Mittal, T. Lund, P. Moin, Study of flow in a planar asymmetric diffuser using large-eddy simulation, J. Fluid Mech. 390 (1) (1999) 151 – 185.

[24] C. U. Buice, J. K. Eaton, Experimental investigation of flow through an asymmetric plane diffuser, Centre for Turbulence Research Annual Research Briefs 1995 (1995) 117 – 120.

[25] A. Hellsten, P. Rautaheimo (Eds.), 8th ERCOFTAC/IAHR/COST Workshop on refined turbulence modelling, ERCOFTAC, Helsinki University of Technology, Espoo, Finland, 1999.

[26] D. Apsley, M. Leschziner, Advanced turbulence modelling of separated flow in a diffuser, Flow, Turbul. Combust. 63 (1-4) (2000) 81–112. doi:10.1023/A:1009930107544.

[27] P. A. Durbin, Separated flow computations with the $k-\epsilon-v^2$ model, AIAA J. 33 (1995) 659–664. doi:10.2514/3.12628.

[28] B. E. Launder, B. I. Sharma, Application of the energy-dissipation model of turbulence to the calculation of flow near a spinning disc, Lett. Heat Mass Trans. 1 (1974) 131–137.